Astronomical Techniques and Instruments, 2026

Open Access

Configuration verification of a high-stability and lightweight intermediate block for the primordial gravitational wave telescope

Yabo Wu[1,2,3*], Zhongyu Yue[1,2], Guomin Wang[1,2,3]

[1]*Nanjing Institute of Astronomical Optics & Technology*, *Chinese Academy of Sciences*, *Nanjing* 210042, *China*

[2]*CAS Key Laboratory of Astronomical Optics & Technology*, *Nanjing Institute of Astronomical Optics & Technology*, *Nanjing* 210042, *China*

[3]*School of Astronomy and Space Science*, *University of Chinese Academy of Sciences*, *Beijing* 100049, *China*

*Correspondence: ybwu@niaot.ac.cn

Received: April 3, 2026; Accepted: May 19, 2026; Published Online: May 20, 2026; https://doi.org/10.3724/ati2026024; https://cstr.cn/32083.14.ati2026024

© 2026 Editorial Office of Astronomical Techniques and Instruments, Yunnan Observatories, Chinese Academy of Sciences. This is an open access article under the CC BY-NC-ND 4.0 license (http://creativecommons.org/licenses/by-nc-nd/4.0/)

Citation: Wu, Y. B., Yue, Z. Y., Wang, G. M. 2026. Configuration verification of a high-stability and lightweight intermediate block for the primordial gravitational wave telescope. *Astronomical Techniques and Instruments*, https://doi.org/10.3724/ati2026024.

Abstract: As the core load-bearing hub connecting the optical payload and the mechanical axis system in the Ali Primordial Gravitational Wave Telescope, the specific stiffness and pointing stability of the intermediate block directly determine observation accuracy in extreme high-altitude environments. To overcome the mass-stiffness trade-off encountered in the 2-m-scale large-span support structure, under stringent assembly space constraints, conventional weight reduction or unconstrained optimization algorithms alone often fall short of engineering manufacturability. We therefore introduce the generalized specific stiffness scaling law as a theoretical basis for structural selection. Combining the extreme physical boundaries of internal routing clearance and multi-point discrete rigid assembly, we deduce and establish an "in-plane tension-compression-dominated" concentric octagonal truss base configuration. Because the traditional maximum deformation metric is highly susceptible to local stress concentrations and cannot accurately characterize the macroscopic deflection of optical components, we use Singular Value Decomposition to spatially fit the discrete nodal displacement field of the load-bearing surface, advancing the evaluation precision of the gravity-induced tilt angle to the arcsecond level. A local parameter space scan, conducted under this precise metric, clearly reveals the high-order shear stiffness gain mechanism of thin-walled stiffening ring plates within confined spaces. Comprehensive comparative data demonstrate that, under equivalent loading boundaries, the optimized truss configuration reduces the structural mass of the base from 1019.52 kg to 536.29 kg (a 47.40% reduction), while the gravity-induced tilt angle decreases from 20.95″ to 11.31″ (improving pointing accuracy by a factor of 1.85). Ultimately, by constructing a systematic strategy of "tension-compression-dominated topology+shear stiffening rings", we can fundamentally overcome the mass-stiffness trade-off in large-span precision structures, providing a practical engineering verification method for large ground-based astronomical telescopes.

Keywords: Primordial gravitational wave telescope; Intermediate block; Micro-tilt angle evaluation; Precision support structure

1. INTRODUCTION

Primordial gravitational waves carry spacetime quantum fluctuation information from the cosmic inflation epoch, serving as key evidence to verify early universe theoretical models and their physical mechanisms. To obtain high-precision Cosmic Microwave Background (CMB) polarization data in the northern sky, China has constructed the Primordial Gravitational Wave Telescope at the Ali site in Tibet, located at an altitude of 5250 m[1−3]. As the core load-bearing component connecting the optical payload and the complex mechanical axis system (including high-precision altitude and azimuth tracking subsystems[4,5]), the intermediate block has a geometric span of 2.2 m[6,7]. Precise control of its structural deformation directly affects the pointing accuracy of the telescope[8−10].

Similar to the gravity-induced deformation observed in large-aperture continuous mirrors[11], large-span precision support structures[12,13] also face a sharp increase in structural self-weight, often accompanied by significant gravity-induced tilt deformation. This inevitably leads traditional solid or thick-walled configurations, which rely on

simple material accumulation, into an inherent mass-stiffness bottleneck. For large-span lightweight designs, mitigating scaling effects by shifting the load-bearing mode from "out-of-plane bending-dominated" to "in-plane tension-compression-dominated" has been validated in numerous engineering applications. However, the design of the intermediate block for the telescope is not a single-objective mathematical optimization. Preliminary engineering investigations indicate that the interior of the structure must reserve an absolutely interference-free clearance for the cryogenic cooling mechanism and complex cabling, while its exterior must match multi-point discrete high-rigidity mechanical connections. Furthermore, constrained by the extreme transportation and on-site assembly capabilities at high altitudes, conventional continuum topology optimization driven by compliance minimization (which often yields theoretical solutions with centralized material accumulation or irregular intersecting grids[14–16]) is highly prone to triggering severe physical interferences and manufacturing bottlenecks during actual assembly.

In response to the failure of traditional configurations caused by multiple spatial and process constraints, in this study, we break through the theoretical limitations of unconstrained optimization and propose a system-level scheme from basic configuration deduction to quantitative verification. Using the generalized specific stiffness scaling law as the theoretical screening criterion and combining it with the actual physical interference matrix, we rigorously deduce an "in-plane tension-compression dominated" concentric octagonal truss topology. Given that the traditional maximum deformation metric cannot objectively characterize the macroscopic deflection of optical components, we introduce Singular Value Decomposition (SVD)[17,18] to spatially fit the discrete nodal displacement field, achieving arcsecond-level analysis of the optical axis micro-tilt angle. Under this evaluation metric, we conduct a local parameter space scan to ascertain the key stiffness gain mechanisms of the main pipe walls and the stiffening ring plates. We then construct a comprehensive specific stiffness index for multi-dimensional quantitative comparison, aiming to provide a rigorous engineering verification path for the highly stable and lightweight design of similar large-scale constrained astronomical telescopes.

2. STRUCTURAL MATHEMATICAL MODEL AND STIFFNESS SCALING LAW CONSTRUCTION

The establishment of a structural mathematical model for the intermediate block does not originate from a simple optimization of mechanical parameters, but is strictly governed by two rigid constraints: Internal physical avoidance and the external manufacturing environment. As the crucial conduit for photoelectric signal processing, the interior of the intermediate block must reserve a large-aperture, absolutely interference-free clearance to accommodate the optical instruments and superconducting refrigeration pipelines. This rigid physical boundary directly precludes the feasibility of a central solid entity or an internal intersecting grid, fundamentally locking the structure into a "hollow" macroscopic scheme.

Simultaneously, the extreme altitude of 5250 m not only brings stringent limitations on hoisting loads, but also eliminates the possibility of high-strength on-site welding. Consequently, the final structural assembly must rely entirely on prefabricated high-precision mechanical interfaces[19]. Compared with complex, irregularly shaped bionic curved surfaces that are prone to machining errors, a polygonal frame structure, primarily composed of standardized straight steel tubes and featuring straight edges, can more stably and efficiently handle significant local stress diffusion at discrete hard points. Through systematic simplification, based on the aforementioned manufacturing and spatial interference matrices, we discretize the ideal continuous ring, making the "inner and outer concentric regular octagonal frame" the only manufacturable fundamental topology in this study.

2.1. Geometric Definition and Physical Model

The main body of the intermediate block adopts an inner and outer concentric regular octagonal steel tube frame structure, as shown in Fig. 1. We establish a Cartesian coordinate system with the origin O at the center of the concentric circles. The X-axis lies in the horizontal direction, the Y-axis in the vertical direction (the direction of gravity), and the Z-axis points perpendicularly outward from the page (the direction of the optical axis).

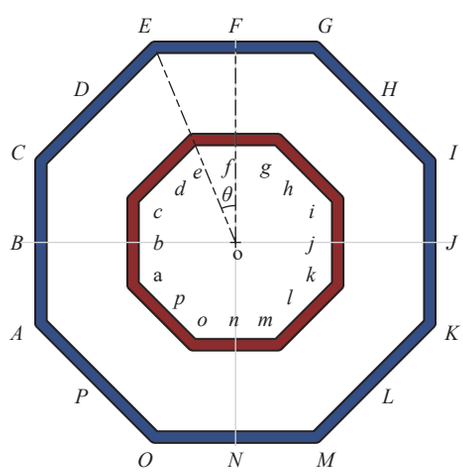


Fig. 1. Schematic diagram of the regular octagonal steel tube frame structure.

To establish our basic mathematical model, we first define the core geometric parameters of the structural framework. For the inner ring (i.e., the load end), the radius of the inscribed circle is $r = 500$ mm, and the node set is denoted as $\boldsymbol{P}_{\text{in}}$. For the outer ring (i.e., the support end), the radius of the inscribed circle is $R = 950$ mm, and the node set is denoted as $\boldsymbol{P}_{\text{out}}$. All members are structural

steel tubes with an elastic modulus, E, a cross-sectional moment of inertia, I, and a linear density, ρ.

Following the geometric definition, we apply specific boundary conditions and external loads, to simulate the actual operating conditions of the telescope. According to the mounting method of the telescope, the upper and lower pole regions of the outer ring (nodes E, F, G, M, N, and O) are defined as a fixed constraint set, reflecting the rigid support provided by the telescope's elevation axis structures. The remaining nodes act as free boundaries.

To simulate the actual operational state, the optical payload of the telescope is modeled as a remote mass of M_p = 1 280 kg. This mass is coupled to the discrete assembly nodes of the inner ring, with its Center of Gravity (CG) located at Z = 1 080 mm along the optical axis (relative to the bottom surface of the intermediate block). The total structural response is evaluated under the combined effect of structural self-weight and the payload gravity field.

2.2. Principle of Minimum Potential Energy

The total potential energy of the system is composed of the strain energy and the potential energy of external forces. According to the principle of minimum potential energy, the true displacement field makes the total potential energy of the system stationary, according to the relation

$$\delta\Pi = \delta(U - W) = 0, \tag{1}$$

where Π is the total potential energy of the system, U is the strain energy, and W is the potential energy of external forces.

In this context, we establish the stiffness equations of the intermediate block under two characteristic postures of the telescope, horizontal and vertical, and derive the stiffness evolution laws under different load-bearing modes.

2.3. Derivation of a Bending Scaling Law for Extreme Out-of-plane Loading

To theoretically isolate the stiffness degradation mechanism of the "out-of-plane bending" mode, we select the zenith-pointing horizontal posture of the telescope as an extreme mathematical boundary condition. Under this specific theoretical boundary, the intermediate block primarily bears the gravity, Q, along the Z-axis. The structure is evaluated under an "out-of-plane bending" stress state, and the inner ring only undergoes a translation, δ_z, along the Z-axis.

2.3.1. *Construction of the energy functional*

Based on Euler-Bernoulli beam theory, the bending strain energy of the i-th effective member connecting the inner and outer rings, when undergoing a relative displacement, is given by

$$U_i = \frac{1}{2}k_{b,i}\delta_z^2 = \frac{1}{2}\left(\frac{12EI}{L_i^3}\right)\delta_z^2, \tag{2}$$

where $k_{b,i}$ is the bending stiffness of the i-th member, L_i is the effective length of the member in m, and δ_z is the translational displacement of the inner ring along the optical axis (Z-axis) in m.

For members connected to non-fixed regions, their stiffness contribution is neglected because of the lack of support reaction forces. The total potential energy of the system can be expressed as

$$\Pi = \sum_{i\in S_{\text{fixed}}} \frac{6EI}{L_i^3}\delta_z^2 - Q\delta_z, \tag{3}$$

where S_{fixed} is the set of effective load-bearing members, and Q is the gravity load borne by the intermediate block in N.

2.3.2. *Equilibrium equation and scaling law*

Taking the variation of Π with respect to Δz, we obtain the equilibrium equation, where the equivalent bending stiffness is

$$K_{\text{eq}} = 12EI \sum_{i\in S_{\text{fixed}}} \frac{1}{L_i^3}. \tag{4}$$

By introducing the specific stiffness efficiency factor, $\eta = K_{\text{eq}}/M_{\text{total}}$, and considering the member mass, $m_i \propto L_i$, we derive the fourth-power scaling law under the bending-dominated condition, given by

$$\eta_{\text{bending}} \propto \frac{1}{L^4}, \tag{5}$$

where η_{bending} is the specific stiffness of the bending-dominated structure and L is the characteristic scale of the structure. This indicates that the specific stiffness of a bending-dominated structure decays with the fourth power of the characteristic scale. This significant scaling effect is the core reason for the mass-stiffness trade-off inherent in traditional solid structures[20].

2.4. Derivation of a Tension-compression Scaling Law for In-plane Loading

To mathematically decouple and extract the stiffness characteristics of the "in-plane tension-compression" mechanism, we similarly utilize the horizontal observation (i.e., vertical posture) as the counterpart extreme boundary. In this state, gravity, Q, acts along the Y-axis, and there is an overturning moment induced by a center-of-gravity offset, t. The structure shows an "in-plane tension-compression" load-bearing state. We treat the inner ring as a rigid body with three in-plane degrees of freedom, $\boldsymbol{q} = [u, v, \theta]^{\mathrm{T}}$.

2.4.1. *Derivation of the stiffness matrix*

The direction vector of the k-th effective member is n_k, its axial stiffness is EA/L_k, and the axial elongation of the member induced by a micro-displacement of the inner ring is Δl_k. Using the variational principle, we derive the linear equilibrium equation system, where the

global stiffness matrix, $\boldsymbol{K}$, of the system is

$$\boldsymbol{K} = \sum_{k \in S_{\text{fixed}}} \frac{EA}{L_k} \begin{bmatrix} \cos^2\theta_k & \cos\theta_k \sin\theta_k & \cdots \\ \cos\theta_k \sin\theta_k & \sin^2\theta_k & \cdots \\ \vdots & \vdots & \ddots \end{bmatrix}, \quad (6)$$

where $\boldsymbol{K}$ is the global stiffness matrix, θ_k is the angle between the k-th member and the horizontal axis in rad, and S_{fixed} is the set of load-bearing members.

2.4.2. *Stiffness solution and tension-compression scaling law*

By solving Equation (6), we can conclude that the axial stiffness of the structure in the tension-compression-dominated loading case is positively correlated with the term EA/L. Together with the scaling relation of mass, $M \propto L$, the quadratic power scaling law applicable to the tension-compression-dominated working condition can be derived as

$$\eta_{\text{axial}} \propto \frac{1}{L^2}, \quad (7)$$

where η_{axial} is the specific stiffness of the tension-compression-dominated structure. Comparing Equation (5) and Equation (7), we can see that the decay rate of η_{axial} with the characteristic scale is much slower than that of η_{bending}. This provides a theoretical basis for employing truss topology optimization to resolve the stiffness problem of large-scale structures.

2.5. Theoretical Summary and Topology Selection Strategy

The aforementioned mathematical derivations establish the fundamental mechanical boundaries governing load-transfer paths. Structures dominated by bending suffer a severe specific stiffness decay of $\eta_{\text{bending}} \propto 1/L^4$, whereas tension-compression-dominated structures exhibit a significantly mitigated scaling effect of $\eta_{\text{axial}} \propto 1/L^2$.

Crucially, to rigorously evaluate the structural performance, both the traditional solid/thick-walled configuration and the novel truss configuration must be compared under the identical most unfavorable boundary condition, i.e., the horizontal posture under Z-axis gravity, where out-of-plane deformation is maximized.

Under this identical severe posture, a traditional macroscopic continuous solid topology inevitably relies on localized plate/shell bending to resist the out-of-plane load, inherently triggering the $1/L^4$ scaling effect and the mass-stiffness trade-off [21–23]. By contrast, the proposed concentric octagonal truss proactively alters the force flow transmission path through its discrete spatial arrangement. Even under extreme out-of-plane loading, the spatial truss network synergistically decomposes the macroscopic bending moments into localized "axial tension-compression" forces along the main structural tubes.

By deliberately enforcing a tension-compression-dominated load transfer mechanism under the same spatial constraints, the intermediate block successfully capitalizes on the $1/L^2$ scaling law. Furthermore, based on this fundamental truss topology, stiffening ring plates are introduced to optimize the local in-plane shear stiffness of the inner ring, fundamentally enhancing the pointing stability of the telescope.

3. STRUCTURAL CONFIGURATION DESIGN AND EVALUATION

Based on the theoretical derivation of the generalized specific stiffness scaling law and the engineering performance requirements of the Ali Primordial Gravitational Wave Telescope, we design three concentric octagonal intermediate block structures with different connection methods. We compare the mass and stiffness characteristics of each scheme through modal analysis to determine the optimal base configuration, and perform a wall thickness sensitivity analysis on the key load-transferring members, to explore the structural lightweight potential.

3.1. Design of Concentric Octagonal Configurations

Based on the tension-compression-dominated design principle, we design three concentric octagonal truss structures with different base connection methods. The core design uses steel tubes as basic components to construct inner and outer concentric octagonal frames, connecting the inner and outer rings with radial and diagonal members, thereby ensuring the structure primarily bears in-plane tension and compression. The difference among the three schemes concerns the connection method of the base radial members: Scheme I connects all radial members except *B-b* and *J-j* (Fig. 2A); Scheme II increases the connection span of the vertical members (Fig. 2B); and Scheme III uses full steel plate welding for the bottom, with all radial stiffening ribs built-in (Fig. 2C).

3.2. Analysis and Comparison of the Three Connection Schemes

For the preliminary evaluation, we assign representative baseline dimensions to each scheme to establish comparable overall mass levels. Specifically for Scheme II, we set the wall thickness of the steel tubes *E-c* and *G-i* to 10 mm, while the remaining tubes are 6 mm. For each scheme, we then perform modal analysis, and the first six natural frequencies are presented in Fig. 3.

The preliminary modal analysis indicates fundamental differences in specific stiffness among the topologies. Scheme III has a significantly higher mass of 1011.8 kg, demonstrating the inherent mass-stiffness limitation of continuous solid configurations.

Although the overall masses of Scheme I (947.4 kg) and Scheme II (942.5 kg) are comparable, Scheme II yields a higher first natural frequency of 43.4 Hz (vs. 41.3 Hz). This performance gap originates from the underlying topological load-transfer mechanism rather than parametric sizing. Under dynamic loading, the radial topol-

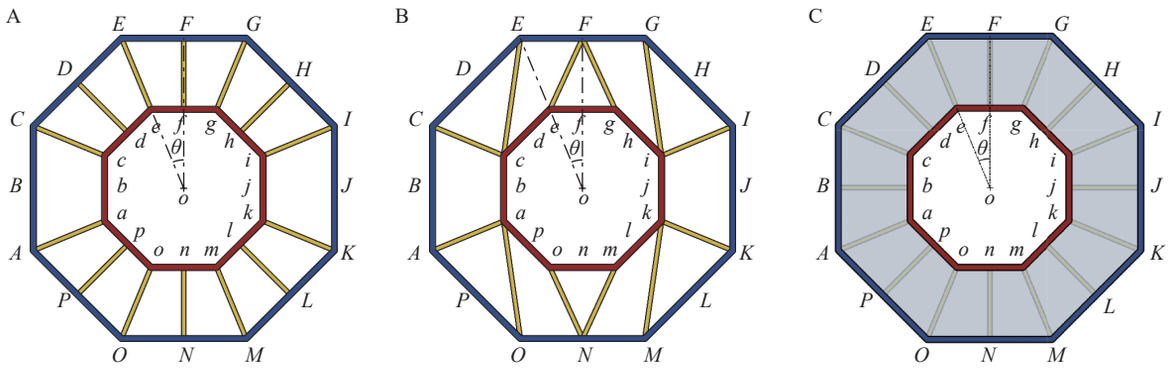


Fig. 2. Concentric octagonal truss connection schemes. (A) Scheme I. (B) Scheme II. (C) Scheme III.

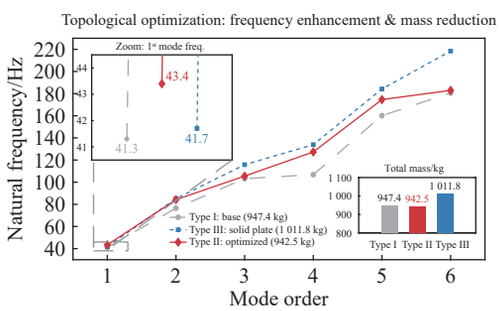


Fig. 3. Modal analysis comparison of the three connection schemes. The main plot shows the first six natural frequencies for each topological configuration. The insets detail the local frequency enhancement at the first-order mode (top left) and compare the total structural mass of the three schemes (bottom right).

ogy of Scheme I relies heavily on localized bending moments at the joints. Conversely, the triangulated network in Scheme II resolves macroscopic bending moments into axial tension and compression forces along the diagonal members.

Increasing the tube wall thickness of Scheme I to match the absolute stiffness of Scheme II would incur a substantial mass penalty, negating its lightweight advantage. Because the triangulated topology of Scheme II physically provides a higher specific stiffness limit, it inherently outperforms Scheme I. Moreover, Scheme II geometrically reserves more space at the base of the intermediate block for cable routing or instrument installation. We therefore select Scheme II as the superior baseline topology for the subsequent detailed parametric optimization.

4. LOCAL PARAMETER SPACE SCAN OF KEY CHARACTERISTIC DIMENSIONS AND STIFFNESS EVOLUTION MECHANISM

From the perspective of physical transmission mechanisms, the wall thickness of the main load-bearing tubes dominates the low-order dynamic stiffness and inertial mass of the system, while the radial span of the ring plates determines the bending moment of inertia and the solid thickness of the ring plates controls the local in-plane shear stiffness. These three factors show a high degree of orthogonal decoupling in their mechanical responses. Based on this mechanical foundation, we conduct a local parameter space scan near the baseline points to accurately ascertain the independent physical contributions of each geometric feature to the micro-tilt angle.

4.1. Decoupling Algorithm for Optical Axis Deviation in Discrete Displacement Fields

Extracting macroscopic optical axis deviations from discrete, complex structural deformation fields is a critical challenge in high-precision optomechanical systems. Recent studies have demonstrated that advanced decoupling algorithms are essential to isolate rigid-body tilts from complex nodal deformations, as explored in space-based precision optical systems[24]. Therefore, for the 2-m-scale concentric octagonal frame, characterized by a massive number of discrete nodes at its load-bearing interfaces, it is imperative to avoid the statistical errors of local nodal stress concentrations inherent in traditional localized measurements.

We employ the SVD algorithm to perform spatial plane fitting and geometric dimensionality reduction on the spatial displacement field of these massive discrete nodes[17,18]. In the calculation procedure, the deformation set of key inner ring nodes is first extracted from finite element static analysis results, and the displacement matrix, $\tilde{\boldsymbol{X}}$, is established via mean-centering processing. SVD is then applied to the matrix, $\tilde{\boldsymbol{X}} = \boldsymbol{U}\Sigma\boldsymbol{V}^{\mathrm{T}}$, where $\boldsymbol{U}$ and $\boldsymbol{V}$ are orthogonal matrices whose columns are the left and right singular vectors, respectively, and Σ is the diagonal matrix of singular values. Geometrically, the right singular vectors in $\boldsymbol{V}$ represent the principal axes of the spatial node distribution, and the singular values in Σ quantify the variance along these axes. Because the inner ring is a shallow planar structure, the direction of least spatial variance corresponds to its normal direction. Therefore, we adopt the right singular vector, corresponding to the minimum singular value, as the normal vector, $\boldsymbol{n}$, of the deformed fitted plane.

By calculating the angle between $\boldsymbol{n}$ and the ideal optical axis, the intricate elastic deformation field can be mapped to a single intuitive gravity-induced optical axis tilt angle θ (see Fig. 4). This dimensionality reduction

explicitly filters out the "data noise" coupled from radial displacements and local high-order warpage. This system avoids the disturbance of the local stress concentration and establishes an arcsecond-level evaluation benchmark for subsequent structural stiffness evolution analysis.

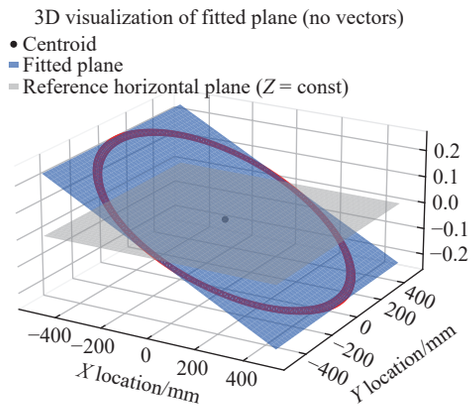


Fig. 4. 3D visualization of the fitted plane, based on the discrete nodal displacement field.

4.2. Nonlinear "Stiffness-mass" Competition of Load-Transferring Skeleton Wall Thickness

To further explore the lightweight potential of the structure, we conduct a detailed wall thickness sensitivity analysis on the four key load-transferring steel tubes connecting the fixed points, *F* and *N*. To keep other structural parameters constant, we investigate how wall thickness varying from 5 mm to 9 mm influences the overall structural stiffness (i.e., first-order natural frequency) and mass. The results are shown in Fig. 5.

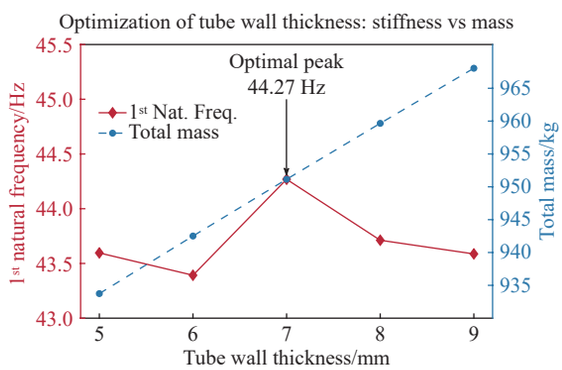


Fig. 5. Nonlinear mechanical competition between dynamic stiffness and structural mass. The plot highlights the optimal frequency peak at 7 mm.

In-depth modal tracking reveals a significant nonlinear mechanical competition. Although the total mass of the structure shows a deterministic linear climb as the wall thickness increases, the first-order frequency characterizing the dynamic stiffness does not increase monotonically. Instead, it exhibits a non-monotonic behavior of "first rising and then falling", reaching a global maximum of 44.27 Hz as the wall thickness approaches 7 mm. This mechanical mutation phenomenon indicates that once the cross-sectional thickness crosses a specific critical point, the sharp increase in local inertial forces introduced by excessive material accumulation generates a negative drag effect on the inherent modes of the system, which offsets the stiffness gain brought by the cross-sectional moment of inertia. On the basis of this physical competition mechanism, we strictly define the optimal wall thickness of the main trunk as 7 mm.

4.3. Analysis of Stiffening and Bending Stiffness

The inner ring of the intermediate block is directly connected to high-precision bearings, and its local stiffness characteristics directly determine the pointing stability of the telescope's optical axis. To suppress the out-of-plane bending deformation in the inner ring region, we introduce continuous annular cover plates (stiffening ring plates) as reinforcement structures. A structural configuration comparison is shown in Fig. 6. To determine the optimal geometric parameters, we conduct sensitivity analyses separately for the radial span (i.e., length) and the plate thickness of the cover plates.

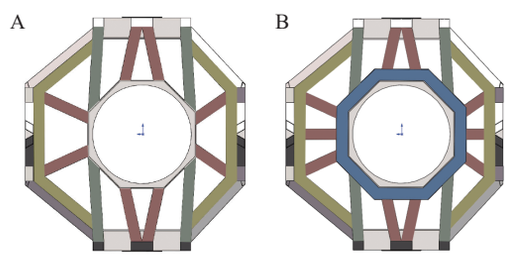


Fig. 6. Intermediate block configurations (A) without stiffening ring plates, and (B) with stiffening ring plates. Note: The color-coding in configuration (B) shows the heterogeneous wall thickness distribution of the final optimized state derived in Section 4.4, with diagonal struts in green, radial straight tubes in red-brown, outer ring tubes in light yellow, and the inner stiffening cover plate in steel blue.

Keeping the plate thickness constant, we investigate how increasing the radial span of the cover plate from 50 mm to 110 mm affects the gravity-induced tilt angle. The evolution law is shown in Fig. 7.

Our calculations indicate that the structural tilt angle decreases monotonically with increasing radial span of the stiffening cover plate, while the stiffness gain efficiency, $|\Delta\theta/\Delta L|$, shows significant attenuation. Within $L \in [50, 70]$ (in mm), the cover plate effectively raises the inner ring's sectional moment of inertia, with an average tilt angle reduction of ~1.28″ per 10 mm. The curve plateaus for $L > 90$ mm, with the 10 mm incremental reduction narrowing to 0.85″ as L rises from 100 mm to 110 mm. This demonstrates that the efficiency of stiffness improvement via pure geometric extension is nearing its physical limit.

Although a further increase in the radial dimension can still bring a slight stiffness improvement, an excessively long overhanging plate/shell will introduce significant parasitic mass, leading to a decrease in the specific stiffness of the structure. More importantly, as the hub of the tele-

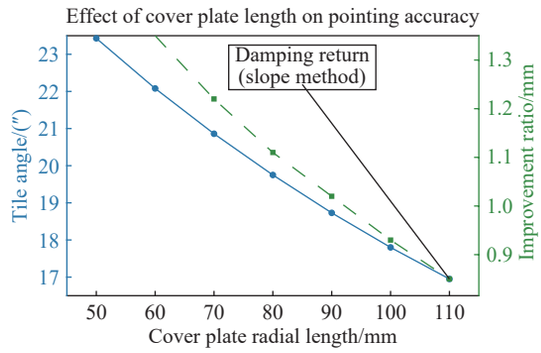


Fig. 7. Relationship between the radial span of the cover plate and the gravity-induced tilt angle. The plot shighlights the saturation effect of structural stiffness improvement as the span approaches 110 mm.

scope, the internal space of the intermediate block must be reserved for cable routing and instrument assembly, and increasing the cover plate width without limit will encroach upon critical maintenance access. Comprehensively considering the saturation of stiffness efficiency and functional space constraints, we set the radial span of the cover plate at 110 mm as the baseline parameter for subsequent design.

4.4. Linear Gain of Stiffening Ring Plate Thickness Effect

Based on determining the radial span to be 110 mm, we further analyze the influence of the cover plate thickness on the pointing accuracy, as shown in Fig. 8.

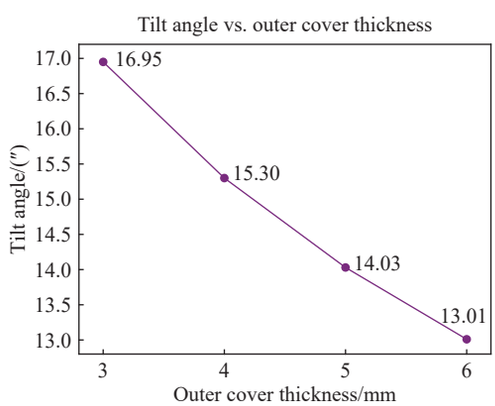


Fig. 8. Relationship between the thickness of the cover plate and the gravity-induced tilt angle.

Unlike the nonlinear saturation observed in the length optimization, the increase in the cover plate thickness demonstrates a near-ideal linear stiffness gain. Data fitting shows that for every 1 mm increase in thickness, the tilt angle decreases by an average of approximately 1.3″.

We attribute this highly efficient stiffness improvement to the stiffening ring plate effect. Increasing the thickness directly enhances the in-plane shear stiffness of the stiffening ring plate, coordinating the deformation of the inner and outer octagonal frames more efficiently and suppressing local warping. Compared with simply adding counterweights or area, increasing the thickness of the stiffening ring plate is the most efficient means to enhance the specific stiffness of large-span truss structures.

After conducting systematic parameter space scans, we can rigorously determine the geometric parameters of the optimized intermediate block. All spatial skeletal members have a standard 200 × 100 mm rectangular steel tube as the base profile. To maximize the specific stiffness, the tube wall thicknesses, t, are heterogeneously distributed based on their functional load-transfer paths. In the optimized model, the diagonal struts, radial straight tubes, and outer ring tubes have thicknesses of 10 mm, 7 mm, and 6 mm, respectively. Concurrently, the inner stiffening cover plate has a final radial span of 110 mm and a solid thickness of 6 mm. Based on the load transfer path analysis, we perform topology optimization on the material distribution along the outer edge of the stiffening ring plate to eliminate inefficient redundant parts in the structure. In the optimized configuration, the base mass of the intermediate block is 536.29 kg, and the overall total mass is 989.97 kg. Its gravity-induced tilt angle converges to 11.31″.

As a comparison, Fig. 9 shows the Z-axis directional deformation of the inner ring for different configurations. The traditional configuration (Fig. 9A), serves as the initial baseline with a base mass of 1019.52 kg, with a solid regular octagonal inner ring to ensure local mounting rigidity, and square steel tubes connecting all outer ring nodes to their corresponding inner ring nodes. By contrast, the optimized configuration (Fig. 9B) replaces the solid ring with a hollow skeleton, enhanced by stiffening plates, fundamentally refining the load transfer paths and minimizing macroscopic deformation.

As in the Z-axis deformation contours, the optimized truss has a reversed tilt direction compared with the baseline, which stems from the shift in the structural center of stiffness, driven by the topological change from continuous plates to a discrete cross-bracing network under asymmetric fixed boundary conditions. More importantly, regardless of the tilt direction, the peak-to-valley (PV) value for the maximum relative Z-axis deformation is significantly decreased. This absolute reduction effectively suppresses the data noise coupled from radial displacements, enhancing the overall pointing accuracy of the telescope.

Fig. 10 shows a quantitative performance comparison between the two configurations, demonstrating that the optimized topology design reduces the base structural mass from 1019.52 kg to 536.29 kg, achieving a weight reduction of 47.40% (with the overall total mass of the optimized intermediate block being 989.97 kg). Simultaneously, the gravity-induced tilt angle is reduced from 20.95″ to 11.31″, improving the pointing accuracy by a factor of 1.85.

5. CONCLUSIONS

Aiming at the significant “mass-stiffness” dilemma of the Ali Primordial Gravitational Wave Telescope intermedi-

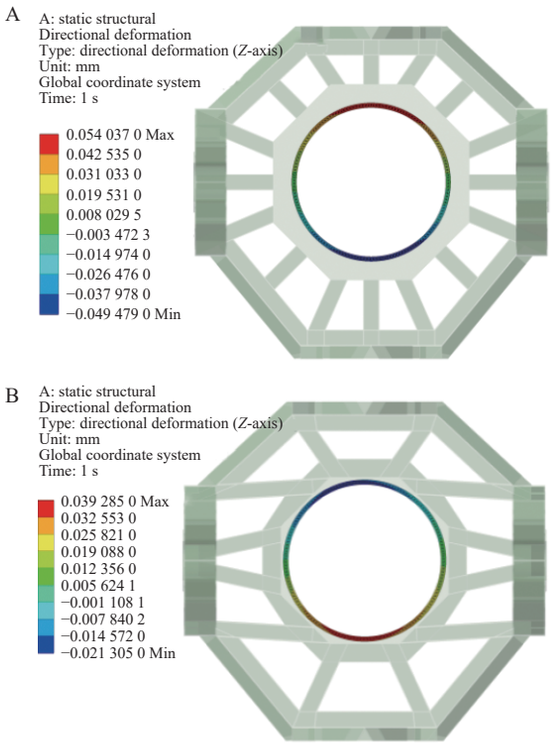


Fig. 9. Directional deformation (*Z*-axis) of the inner ring. (A) traditional configuration; (B) optimized configuration.

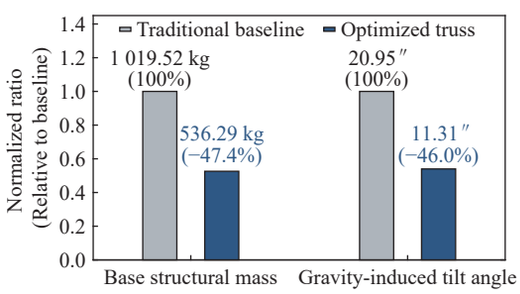


Fig. 10. Comparison of the base structural mass and gravity-induced tilt angle between the traditional baseline and the optimized truss.

ate block at the 2-m scale, we propose a topological configuration optimization method guided by the generalized specific stiffness scaling law and conduct systematic verification combined with the SVD micro-tilt angle evaluation system. We draw three main conclusions.

We have elucidated the underlying theoretical mechanisms of load transfer. Our derivation, based on the principle of minimum potential energy, proves that the structural specific stiffness decays sharply at a rate of L^{-4} under the "out-of-plane bending-dominated" mode, while it decays only at L^{-2} under the "in-plane tension-compression-dominated" mode. This scaling law elucidates the physical necessity of transforming the intermediate block from a solid or thick-walled structure to a concentric octagonal truss structure, establishing the design principle of maximizing specific stiffness by altering the force flow transmission path.

We find that optimizing the topology yields significant performance improvements. Numerical simulations and comparative analyses show that, under the premise of ensuring pointing accuracy, the base structural mass of the optimized truss structure is reduced from 1019.52 kg to 536.29 kg (a 47.4% weight reduction) compared with similar conventional configurations. Meanwhile, the gravity-induced tilt angle is reduced from 20.95″ to 11.31″, improving pointing accuracy by a factor of 1.85. This shows that the "tension-compression-dominated topology" shows excellent efficacy in the design of precision support structures.

Our proposed optimization strategy can be broadly applied to a variety of engineering contexts. Our optimization strategy, proposing the combination of "scaling law theoretical guidance" and "shear enhancement via stiffening ring plates", not only successfully solves the engineering challenges of large-span, high-altitude, and high-precision support structures in this project, but also provides general theoretical references and methodological support for the lightweight and high-stability design of other large ground-based telescopes.

ACKNOWLEDGEMENTS

This work was supported by the National Key R&D Program of China (Development of three-dimensional high-speed rotating platform, 2021YFC2203302).

AI DISCLOSURE STATEMENT

Deepseek and Doubao were employed for language and grammar checks of the article. The authors carefully reviewed, edited, and revised the texts generated by these tools in line with their own preferences, and assume ultimate responsibility for the content of the publication.

AUTHOR CONTRIBUTIONS

Yabo Wu took charge of conceptualization, methodology design, theoretical derivation, numerical simulations, as well as the composition of the original draft of this paper. Zhongyu Yue was responsible for supervision, methodology validation, and revision of the manuscript. Guomin Wang completed the work including project administration, funding acquisition, and overall supervision. All authors have read and approved the final manuscript.

DECLARATION OF INTERESTS

The authors declare no competing interests.

REFERENCES

[1] Zhang, X. M., Su, M., Li, H., et al. 2016. The origin of the universe and the Ali primor dialgravitational waves detection. *Physics*, **45**(5): 320−326. (in Chinese)

[2] Li, H., Li, S. Y., Liu, Y., et al. 2019. Probing primordial

gravitational waves: Ali CMB Polarization Telescope. *National Science Review*, **6**(1): 145−154.
[3] Dou, J. Z., Wei, Y. T., Li, H., et al. 2024. Forecast of CMB TB and EB correlations for AliCPT-1. *Journal of Cosmology and Astroparticle Physics*, **10**: 046.
[4] Yue, Z. Y., Jiang, C. Y., Xu, J., et al. 2025. Structural scheme and control strategy of elevation axis for environmental protection cover of primordial gravitational wave telescope. *Infrared and Laser Engineering*, **54**(1): 20240464. (in Chinese)
[5] Zheng, B., Wang, G. M., Wu, Y. B., et al. 2025. Mechanical properties of the unloading electromagnet for Azimuth shaft on the gravitational wave detection telescope. *Machine Design and Research*, **41**(5): 248−253. (in Chinese)
[6] Lin, J. J., Wang, G. M., Chen, W., et al. 2017. Design and optimization of multi-tube telescope center section. *Machine Design and Research*, **33**(4): 171−174. (in Chinese)
[7] Cheng, J. Q. 2003. Principles and design of astronomical telescopes. Beijing: China Science and Technology Press. (in Chinese)
[8] Lü, Z. X., Yu, Z. H., Yang, Y. L., et al. 2023. Development of high sensitivity rain and snow sensor in LHAASO-WFCTA. *Astronomical Research and Technology*, **20**(6): 583−590. (in Chinese)
[9] Li, Y., Li, X. Y., Yang, S. H., et al. 2025. An optimization strategy for reliable Antarctic telescope control systems. *Astronomical Techniques and Instruments*, **2**(6): 366−374.
[10] Wang, X. W., Yu, Y., Xu, Z. B., et al. 2023. Design and assessment of a micro-nano positioning hexapod platform with flexure hinges for large aperture telescopes. *Optics Express*, **31**(3): 3908−3926.
[11] Wang, Z. C., Chen, T., Cao, Y. Y., et al. 2024. The optimization design of a lightweight 2 m SiC mirror for ground-based telescopes. *Photonics*, **11**(6): 581.
[12] Zhao, H. C., Zhang, J. X., Yang, F., et al. 2017. Secondary mirror supporting structure for 1.2 m telescope. *Optics and Precision Engineering*, **25**(10): 2614−2619. (in Chinese)
[13] Shao, L., Yang, F., Wang, F. G., et al. 2012. Optimization design of support system for 1.2 m lightweight SiC primary mirror. *Chinese Optics*, **5**(3): 229−234. (in Chinese)
[14] Luo, Z., Chen, L. P., Huang, Y. Y., et al. 2004. Topological optimization design for continuum structures. *Advances in Mechanics*, **34**(4): 463−476. (in Chinese)
[15] Bendsøe, M. P., Sigmund, O. 2003. Topology optimization: theory, methods, and applications. Berlin: Springer.
[16] Liu, S. T., Hu, R., Zhou, P., et al. 2013. Topologic optimization for configuration design of web-skin-type ground structure based large-aperture space mirror. *Optics and Precision Engineering*, **21**(7): 1803−1810. (in Chinese)
[17] Golub, G. H., Reinsch, C. 1970. Singular value decomposition and least squares solutions. *Numerische Mathematik*, **14**(5): 403−420.
[18] Arun, K. S., Huang, T. S., Blostein, S. D. 1987. Least-squares fitting of two 3-D point sets. *IEEE Transactions on Pattern Analysis and Machine Intelligence*, **PAMI-9**(5): 698−700.
[19] Fan, Z. H., Mu, X. K., Kang, H., et al. 2025. Prediction and uncertainty-based optimization of assembly accuracy for opto-mechanical components with multi-fidelity modeling. *Journal of Mechanical Design*, **147**(11): 111701.
[20] Gibson, L. J., Ashby, M. F. 1997. Cellular solids: structure and properties. Cambridge: Cambridge University Press.
[21] Li, B. H., Luo, J., Qiu, M. Y., et al. 2023. Design technology of the truss support structure of the ultra-low thermal deformation gravitational wave detection telescope. *Opto-Electronic Engineering*, **50**(11): 230155. (in Chinese)
[22] Long, J. J., Sun, L. J., Zhu, Y. Q., et al. 2025. Mirror design based on topology optimized high stiffness lattice. In Proceedings of SPIE, 13799: 1379913.
[23] Xu, J. Q., Wang, G. M., Cui, X. Q., et al. 2018. Design and optimization of truss tube based on giant telescope. *Acta Astronomica Sinica*, **59**(6): 52−60. (in Chinese)
[24] Luo, J., Song, J., Fang, S. J., et al. 2024. Decoupling and noise analysis of multi-degree-of-freedom deformation measurement method for space gravitational wave detection telescope. *Opto-Electronic Engineering*, **51**(2): 82−96. (in Chinese)